THE ASTROPHYSICAL JOURNAL, 205:499–519, 1976 April 15

RADIATIVE SHOCK DYNAMICS. I. THE LYMAN CONTINUUM

RICHARD I. KLEIN* AND ROBERT F. STEIN†
Joint Institute for Laboratory Astrophysics, University of Colorado and National Bureau of Standards
AND
WOLFGANG KALKOFEN
Center for Astrophysics, Harvard College Observatory and Smithsonian Astrophysical Observatory
Received 1975 February 17; revised 1975 May 5

ABSTRACT

We investigate the shock produced by a constant-velocity piston moving into an atmosphere in radiative, hydrostatic, and statistical equilibrium. Self-consistent numerical solutions are obtained to the equations of hydrodynamics, radiative transfer, and level population. Only Lyman continuum radiation is considered. The results are interpreted in terms of the relaxation lengths for the collisional and radiative processes, and by comparing the "radiative" case both with one in which only collisional transitions occur and with the adiabatic case.

The shock quickly develops a temperature spike. At large optical depth, the spike structure is controlled by collisional ionization and three-body recombination. When the shock approaches $\tau_{912} \approx 200$, precursor radiation drives an ionization front rapidly through the remaining atmosphere. At small optical depth, escape of recombination radiation narrows the temperature spike. Low postshock densities in the upper atmosphere reduce the three-body recombination rate and produce a large plateau of nearly constant ionization behind the shock.

Subject headings: hydrodynamics — radiative transfer — shock waves — stars: atmospheres

I. INTRODUCTION

This paper is the first in a series investigating coupled non–LTE radiative transfer and nonlinear hydrodynamics. Here we consider a shock propagating out through an atmosphere of pure hydrogen, with the hydrogen atoms having one bound level and a continuum. Subsequent papers will investigate more complicated atomic models and will apply the techniques developed here to various astrophysical problems. For instance, knowledge of the interaction of fluid motion and radiation may be helpful in understanding (1) the time behavior of the H and K line profiles of Ca^+ in the solar atmosphere, where observations indicate waves moving through the line-formation layers, (2) the emergent spectrum of pulsating stars with shocks in their atmospheres, (3) flare stars with rapid increases in luminosity followed by slow decay, (4) the evolution of supernova remnants, and (5) the formation of compact H II regions in dense clouds.

Previous research in radiation gas dynamics has not considered the fully coupled time-dependent problem. Those investigators who have treated hydrodynamics in its full nonlinear, time-dependent form have generally made severe approximations for the radiation, solving the transfer equation in either the diffusion or the optically thin limits. Those who have calculated radiative transfer in detail have generally studied only steady flow or have assumed a given velocity field.

Vincenti and Baldwin (1962) studied the propagation of small-amplitude acoustic waves in a radiating gray LTE gas using the Eddington approximation. Baldwin and Heaslet (1963) were among the first to investigate steady shock structure with radiative transfer, again in the gray, LTE Eddington approximation. The same problem was studied by Whitney and Skalafuris (1963), but for a hydrogen atom with one bound state and a continuum. Steady shock structure with nonequilibrium radiation and ionization was investigated by Nelson and Goulard (1968). Kalkofen and Whitney (1971) were the first to treat line formation for a two-level atom in a steady shock. In his calculations of stellar pulsation, Christy (1964) solved the full nonlinear hydrodynamics, using a diffusion approximation for the radiation. Hill (1972) extended this work to include transfer effects in the gray, LTE Eddington approximation.

Here we solve simultaneously the nonlinear hydrodynamic equations, the transfer equation for Lyman continuum radiation, and the time-dependent population equation for atoms with one bound level and a continuum. In § II we describe the calculation, and in § III we discuss the results for a piston-driven shock propagating through a static atmosphere in radiative and statistical equilibrium. The approximations made in the calculation are discussed in Appendix A.

* This research was presented to the Department of Physics, Brandeis University, in partial fulfillment of the requirement of the degree of Doctor of Philosophy.

† Visiting Fellow, on leave from Brandeis University, 1973–1974.

II. DESCRIPTION OF THE CALCULATION

We analyzed a constant-velocity piston moving at 4 km s^{-1} (40 percent of local sound speed) into an atmosphere that was in radiative, hydrostatic, and statistical equilibrium. Energy transfer by radiation in the Lyman continuum was included. The possibility of transferring radiation at frequencies with very different opacity will significantly affect the propagation of the shock, and we will consider the case of several continua in the next paper. This poses no new mathematical difficulties, but greatly increases the computation time, which scales as the cube of the number of frequency points.

The nonlinear hydrodynamic equations describing conservation of mass, momentum, and energy were written in terms of a Lagrangian variable and were solved by using finite-difference equations with artificial viscosity (Richtmyer and Morton 1967). The radiative transfer was treated in differential equation form. The first-order transfer equation for the specific intensity was transformed into a second-order differential equation (Feautrier 1964), which was solved implicitly together with the energy equation and the population-rate equations by Newton-Raphson iteration (complete linearization of all variables) (Auer and Mihalas 1969). The column mass was used as the independent variable in both the hydrodynamic and the radiative equations.

We used the following notation:

ρ = mass per unit volume, E = internal energy per unit mass,

I = ionization energy per unit mass, P = pressure,

T = kinetic temperature, U = fluid velocity,

g = acceleration due to gravity, m = mass cm^{-2},

R = fluid displacement, τ = optical depth,

$I_\nu(\tau, \mu)$ = specific monochromatic intensity, $J_\nu = \frac{1}{2}[I_\nu(\tau, \mu) + I_\nu(\tau, -\mu)]$,

χ_ν = absorption coefficient including scattering, $\omega_\nu = \chi_\nu/\rho$ = absorption coefficient,

η_ν = emission coefficient excluding scattering, n_1 = number of neutral hydrogen atoms per unit volume,

n_e = number of electrons per unit volume,

n_1^* = number of neutral hydrogen atoms in LTE per unit volume (defined by the Saha equation in terms of n_e and T),

R_{1K}, R_{K1}' = photoionization and photorecombination frequencies, C_{1K} = collisional ionization frequency,

$\mathscr{H}$ = net rate of radiation-energy absorption per unit volume,

σ_e = Thomson-scattering cross section, Q = artificial viscosity.

a) Basic Equations

The fluid and radiation equations, in one-dimensional plane-parallel geometry, are as follows:

Conservation of momentum:

$$\frac{\partial U}{\partial t} = -\frac{\partial}{\partial m}(P + Q) - g\,. \tag{1}$$

Fluid velocity:

$$U = \partial R/\partial t\,. \tag{2}$$

Conservation of mass:

$$\frac{\partial R}{\partial m} = \frac{1}{\rho}\,. \tag{3}$$

Conservation of energy:

$$\frac{\partial E}{\partial t} + \frac{\partial I}{\partial t} + (P + Q)\frac{\partial(1/\rho)}{\partial t} = \frac{\mathscr{H}}{\rho}\,. \tag{4}$$

Transfer of radiation in the Eddington approximation:

$$\mu^2 \frac{1}{\omega_\nu}\frac{\partial}{\partial m}\left(\frac{1}{\omega_\nu}\frac{\partial J_\nu}{\partial m}\right) = J_\nu - \frac{\eta_\nu}{\chi_\nu} - \frac{n_e\sigma_e J_\nu}{\chi_\nu}\,, \tag{5}$$

where

$$\mu = 1/\sqrt{3}\,.$$

Rate equation:

$$\frac{\partial(n_1/\rho)}{\partial t} + \frac{1}{\rho}\left[n_1(R_{1K} + C_{1K}) - n_1^*(R_{K1}' + C_{1K})\right] = 0\,. \tag{6}$$

This set of coupled nonlinear partial differential equations is supplemented by the following auxiliary relations:
Ionization energy per gram:

$$I = n_e\chi_H/\rho\,, \tag{7}$$

where χ_H = hydrogen ionization potential.
Specific internal energy:

$$E = \frac{3}{2}\frac{kT}{m_H}\left(1 + \frac{m_H n_e}{\rho}\right)\cdot \tag{8}$$

Equation of state:

$$P = \frac{kT\rho}{m_H}\left(1 + \frac{m_H n_e}{\rho}\right)\cdot \tag{9}$$

Energy gained by the fluid from the radiation field per unit volume per unit time:

$$\mathscr{H} = 4\pi\int_{\nu_{\rm Lyman}}^{\infty}(\chi_\nu - n_e\sigma_e)J_\nu d\nu - 4\pi\int_{\nu_{\rm Lyman}}^{\infty}\eta_\nu d\nu\,. \tag{10}$$

Expressions for χ_ν, η_ν, R_{1K}, R_{K1}', and C_{1K} can be found in Auer and Mihalas (1969). The momentum equation does not include momentum transfer from the photons to the gas (radiation pressure), because it is negligible. The radiative-transfer equations were solved in the Eddington approximation, i.e., with one angle point. This simplification is purely one of computational expediency; the inclusion of several angle points poses no difficulties. The angle approximation was expected to be sufficiently accurate for continuum calculations. Electron scattering was negligible at the temperatures considered and was ignored in these calculations.

Note that in time-dependent radiative transfer, the energy equation (eq. [4]) replaces the equation of radiative equilibrium, $\mathscr{H} = -\nabla\cdot F = 0$ (constancy of radiative flux). If $\mathscr{H}$ in equation (4) is positive, the fluid is heated; i.e., it absorbs more energy than it emits. If $\mathscr{H}$ is negative, the fluid radiates more energy than it absorbs (radiative cooling). The rate equation also differs from its statistical-equilibrium counterpart in static atmospheres. We can write equation (6) as

$$\frac{\partial n_1}{\partial t} + n_1\nabla\cdot U + \left[n_1(R_{1K} + C_{1K}) - n_1^*(R_{K1}' + C_{1K})\right] = 0\,, \tag{11}$$

where $\partial n_1/\partial t$ is the Lagrangian time derivative, and $n_1\nabla\cdot U$ represents compression due to differential fluid motion. In a steady, nonmoving atmosphere, $\partial n_1/\partial t = n_1\nabla\cdot U = 0$. Thus, we recover the condition of statistical equilibrium, which balances the rate of ionization to the continuum against the rate of recombination from the continuum.

Two important approximations were made to these equations: (1) we neglected the finite time of photon flight in the transfer equation, and (2) we assigned a common temperature to all components of the plasma. These approximations are discussed in detail in the Appendix.

b) Solution Using Finite-Difference Equations

The coupled set of radiative-hydrodynamic differential equations was transformed into a set of finite-difference equations on a grid of N layers covering the stellar atmosphere, with 10 layers per scale height. The variables describing the gas and the radiation field (P, Q, ρ, E, I, T, n_1, n_e, $\mathscr{H}$, J_ν) are defined at integral time steps and mass zone centers. Position R and fluid velocity U are defined at zone boundaries, with position at integral and velocity at half-integral times. Subscripts refer to space; superscripts, to time.

The fluid-difference equations are, with slight modification, those used by Christy (1964).
Conservation of momentum:

$$\frac{U_l^{n+1/2} - U_l^{n-1/2}}{\Delta t^n} = -g - \frac{P_{l+1/2}^{n+\lambda} - P_{l-1/2}^{n+\lambda} + Q_{l+1/2}^{n-1/2} - Q_{l-1/2}^{n-1/2}}{\Delta m_l}\,, \tag{12}$$

where $\Delta m_{l+1/2} = m_{l+1} - m_l$, $\Delta m_l = \frac{1}{2}(\Delta m_{l+1/2} + \Delta m_{l-1/2})$, $\Delta t^{n+1/2} = t^{n+1} - t^n$, and $\Delta t^n = \frac{1}{2}(\Delta t^{n+1/2} + \Delta t^{n-1/2})$; the pressure at the correctly centered time is given by the Taylor series:

$$P_{l+1/2}^{n+\lambda} = P_{l+1/2}^{n} + \frac{1}{4}\frac{\Delta t^{n+1/2} - \Delta t^{n-1/2}}{\Delta t^{n-1/2}}\left(P_{l+1/2}^{n} - P_{l+1/2}^{n-1}\right);$$

and the artificial viscosity is

$$Q_{l+1/2}{}^{n+1/2} = \frac{4}{(1/\rho_{l+1/2}{}^{n+1}) + (1/\rho_{l+1/2}{}^{n})}(U_{l+1}{}^{n+1/2} - U_l{}^{n+1/2})^2$$

if

$$\rho_{l+1/2}{}^{n} < \rho_{l+1/2}{}^{n+1} \quad \text{and} \quad U_{l+1}{}^{n+1/2} < U_l{}^{n+1/2},$$

or

$$Q_{l+1/2}{}^{n+1/2} = 0$$

otherwise. We centered the momentum equation in time to account for the fact that typically, $\Delta t^{n+1/2} \neq \Delta t^{n-1/2}$. Fluid velocity:

$$\frac{R_l{}^{n+1} - R_l{}^{n}}{\Delta t^{n+1/2}} = U_l{}^{n+1/2}. \tag{13}$$

Conservation of mass:

$$\rho_{l+1/2}{}^{n+1} = \frac{\Delta m_{l+1/2}}{R_{l+1}{}^{n+1} - R_l{}^{n+1}}. \tag{14}$$

Conservation of energy:

$$E_{l+1/2}{}^{n+1} - E_{l+1/2}{}^{n} + I_{l+1/2}{}^{n+1} - I_{l+1/2}{}^{n} + [\tfrac{1}{2}(P_{l+1/2}{}^{n+1} + P_{l+1/2}{}^{n}) + Q_{l+1/2}{}^{n+1/2}]\left(\frac{1}{\rho_{l+1/2}{}^{n+1}} - \frac{1}{\rho_{l+1/2}{}^{n}}\right) = \Delta t^{n+1/2}\frac{\mathscr{H}_{l+1/2}{}^{n+1} + \mathscr{H}_{l+1/2}{}^{n}}{\rho_{l+1/2}{}^{n+1} + \rho_{l+1/2}{}^{n}}. \tag{15}$$

The equation of radiative transfer (Auer and Mihalas 1969) for each frequency can be written:

$$\frac{1}{3}\frac{J_{\nu,l-1/2}}{\Delta\tau_l\Delta\tau_{l+1/2}} - \frac{1}{3}\frac{J_{\nu,l+1/2}}{\Delta\tau_{l+1/2}}\left(\frac{1}{\Delta\tau_{l+1}} - \frac{1}{\Delta\tau_l}\right) + \frac{1}{3}\frac{J_{\nu,l+3/2}}{\Delta\tau_{l+1}\Delta\tau_{l+1/2}} = J_{\nu,l+1/2} - \frac{\eta_{\nu,l+1/2}}{\chi_{\nu,l+1/2}} - \frac{n_{e,l+1/2}\sigma_e J_{\nu,l+1/2}}{\chi_{\nu,l+1/2}}. \tag{16}$$

Note that our differencing scheme defines the ratiation field not at zone boundaries, but rather at midpoints. The consequences of this on the boundary conditions will be discussed later. The centered optical-depth operators were defined as

$$\Delta\tau_l = \tfrac{1}{4}(\omega_{l-1/2} + \omega_{l+1/2})(\Delta m_{l+1/2} + \Delta m_{l-1/2}),$$

$$\Delta\tau_{l+1} = \tfrac{1}{4}(\omega_{l+1/2} + \omega_{l+3/2})(\Delta m_{l+3/2} + \Delta m_{l+1/2}),$$

$$\Delta\tau_{l+1/2} = \tfrac{1}{2}(\Delta\tau_{l+1} + \Delta\tau_i).$$

Rate equation:

$$\frac{(n_1/\rho)_{l+1/2}{}^{n+1} - (n_1/\rho)_{l+1/2}{}^{n}}{\Delta t^{n+1/2}} + \frac{(An_1 - B)_{l+1/2}{}^{n+1} + (An_1 - B)_{l+1/2}{}^{n}}{\rho_{l+1/2}{}^{n+1} + \rho_{l+1/2}{}^{n}} = 0, \tag{17}$$

where

$$A = R_{1K} + C_{1K}, \qquad B = n_1{}^{*}(R_{K1}{}' + C_{1K}).$$

All frequency integrals in $\mathscr{H}$, R_{1K}, and $R_{K1}{}'$ were replaced by quadrature sums. We used a Simpson's rule integration and obtained good accuracy with five points in the continuum. The distribution of the frequency points was chosen so as to minimize the error in the evaluation of rate integrals over a range from 10,000 to 40,000 K, by comparing the frequency integral over the Planck function with the exact result for constant Gaunt factor.

We solved equations (12), (13), and (14) *explicitly* for the velocity, displacement, and density. The energy equation (15), the equations of radiative transfer (16), and the rate equations (17), with the additional constraint that the total density is the sum of the individual component densities, were solved *implicitly* by Newton-Raphson iteration (complete linearization). In this method (Auer and Mihalas 1969), the coupled nonlinear algebraic finite-difference equations were linearized by separating all variables into two parts, $\psi^{i+1} = \psi^i + \delta\psi^i$, where ψ^i is the current estimate (ith iteration) and $\delta\psi^i$ is the first-order correction:

$$\psi \text{ (solution vector)} = \text{col. } (J_1, J_2, \ldots, J_{NK}, T, n_e, n_1),$$

where NK is the number of discrete frequency points in the Lyman continuum. The set of linearized equations formed a block tridiagonal matrix that can be written in the form

$$-A_{l+1/2}\delta\Psi_{l-1/2} + B_{l+1/2}\delta\Psi_{l+1/2} - C_{l+1/2}\delta\Psi_{l+3/2} = L_{l+1/2} \tag{18}$$

for $l = 2, \ldots, N-2$, where A, B, and C are square matrices of order $(NK+3) \times (NK+3)$ and L is a vector of order $(NK+3)$. We employed a Gaussian elimination scheme to solve this system of equations, with suitable boundary conditions, for the first-order corrections to all variables. The corrections $\delta\Psi$ were then used to improve the current estimates, and the entire iteration procedure was continued until a converged solution was obtained. A lambda iteration using the updated temperatures was employed between complete linearization cycles to calculate a smooth radiation field and populations. Initial guesses to the variables at a given time step were obtained by linear extrapolation of the variables from the two previous times.

After a converged model was obtained at the new time t^{n+1}, a new time step was calculated from the Courant condition and from the requirement that all variables change by less than some given fraction between the times t^n and t^{n+1}. Newly calculated quantities were stored in core for extrapolation, and the cycle was repeated for the time t^{n+2}.

The convergence properties of a complete linearization cycle depend sensitively on the initial estimates available on entering the cycle, and the estimates themselves depend on the size of the time step. Typically, a time step can be chosen that is 40–50 percent of the Courant time and that permits the temperature to change by as much as 10 percent, except when the radiation field has steep gradients. When that occurred, as during the propagation of the ionization front, it was found necessary to limit the change in temperature of any zone between t^n and t^{n+1} to $\Delta T/T < 0.005$. At each time step, the model was found to converge rapidly. It was usually converged to relative corrections of less than 1 part in 10^6 in two to three iterations. Over the time spanned by the calculation of 1000 time steps, total energy was conserved to an accuracy of 0.005.

c) *Boundary Conditions*

The velocity and radiation fields on the boundaries were not determined by the above finite-difference equations. At the upper boundary we used the condition that there was no incoming radiation, $I_\nu(\tau_N, -\mu) = 0$. This condition, together with the transfer equation

$$\frac{\mu \partial J}{\partial \tau} = \tfrac{1}{2}(I_+ - I_-) \tag{19a}$$

$$= J - I_- \tag{19b}$$

$$= I_+ - J\,, \tag{19c}$$

provides a relation between J_ν on the boundary and J_ν one step inside the atmosphere. Following Auer (1967), this relation can be expressed to any desired degree of accuracy by writing a Taylor expansion away from the boundary and retaining higher order terms as accuracy demands. That is,

$$J_{N-3/2} = J_{N-1/2} + \left.\frac{\partial J}{\partial \tau}\right|_{N-1/2} \Delta_1 + \left.\frac{\partial^2 J}{\partial \tau^2}\right|_{N-1/2} \frac{\Delta_1^2}{2!} + \cdots\,, \tag{20}$$

where N is the index of the top boundary and

$$\Delta_1 \equiv \tfrac{1}{4}(\omega_{N-3/2} + \omega_{N-1/2})(m_N - m_{N-2})\,.$$

We evaluated $(\partial J/\partial \tau)_{N-1/2}$ by using the first-order equation (19b) at $N - \frac{1}{2}$. Here, $I_-(N - \frac{1}{2})$ is the incoming radiation that reaches zone $N - \frac{1}{2}$, so that $I_- \approx \Delta\tau(\eta_{N-1/2}/\chi_{N-1/2}) + (1 - \Delta\tau)$ times the incoming radiation to the surface, or

$$I_-(N - \tfrac{1}{2}) \approx \Delta\tau(\eta_{N-1/2}/\chi_{N-1/2})\,, \tag{21}$$

where $\Delta\tau = -\omega_{N-1/2}(m_N - m_{N-1/2})$. We evaluated the second derivative in equation (20) by using the transfer equation evaluated at zone $N - \frac{1}{2}$; hence,

$$\mu^2 \left.\frac{\partial^2 J}{\partial \tau^2}\right|_{N-1/2} = J_{N-1/2} - \frac{\eta_{N-1/2}}{\chi_{N-1/2}} - \frac{n_{e,N-1/2}\sigma_e}{\chi_{N-1/2}} J_{N-1/2}\,. \tag{22}$$

(Note that $\partial\tau = -\omega\partial m$.) From equations (19b), (20), and (22), we obtain

$$J_{N-3/2} = J_{N-1/2}\left[1 + \frac{\Delta_1}{\mu} + \frac{\Delta_1^2}{2\mu^2}\left(1 - \frac{n_e\sigma_e}{\chi}\right)_{N-1/2}\right] - \Delta\tau \frac{\eta_{N-1/2}}{\chi_{N-1/2}} \frac{\Delta_1}{\mu} - \frac{\Delta_1^2}{2\mu^2} \frac{\eta_{N-1/2}}{\chi_{N-1/2}}\,. \tag{23}$$

This boundary condition can be linearized in terms of corrections to the basic variables and in a form similar to equation (18).

Calculations for problems with exact solutions have revealed that the accuracy of the solution at the surface depends on the value of the optical depth of the first zone. This sensitivity stems from the approximate way in

which we wrote our upper boundary condition. In evaluating the terms in the Taylor series, we must approximate the radiation from the top half-zone of the atmosphere. The approximation becomes less accurate as the first interior zone is taken farther from the upper boundary. Relative errors in $J_\nu(\tau)$ as large as 10 percent were found when $\tau_{N-1/2} = 0.1$. With $\tau_{N-1/2} = 10^{-4}$, the relative error in J_ν was 0.1 percent. The errors decayed exponentially into the atmosphere. In general, the second-order boundary condition was more accurate than a first-order condition.

At the bottom boundary, different radiative-transfer boundary conditions were used in the equilibrium and time-dependent calculations. In the equilibrium atmosphere, we specified the net radiative flux. In finite-difference form, equation (19c) becomes

$$\frac{J_{3/2} - J_{5/2}}{\frac{1}{4}(m_3 - m_1)(\omega_{5/2} + \omega_{3/2})} = \frac{I_+ - J_{3/2}}{\mu} . \tag{24}$$

Here,

$$I_+(\tau_N) = B_\nu(\tau_N) + \mu \left.\frac{\partial B_\nu}{\partial \tau_\nu}\right|_{\tau_N} , \tag{25}$$

where $\partial B_\nu/\partial \tau_\nu$ is written such that the specified net flux is transported across the bottom boundary of the atmosphere (Auer and Mihalas 1969):

$$\frac{\partial B_\nu}{\partial \tau_\nu} = \frac{3}{\chi_\nu}\frac{\partial B_\nu}{\partial T}\left[\frac{\text{Flux}}{4\pi} + \sum_{i=1}^{NK} \omega_i \mu (J_i - B_i)\right] \Bigg/ \left[\sum_{i=1}^{NK} (\omega_i/\chi_i)(\partial B_i/\partial T)\right] . \tag{26}$$

Radiative equilibrium demands that the flux be constant over the entire atmosphere. The boundary condition (eq. [24]) couples the incoming intensity I_+ at a given frequency to the radiation field at all other frequencies. Linearization of equation (24) in terms of relative corrections is straightforward, but laborious.

In the dynamic calculations, if the incident radiation is constant in time, the net flux across the bottom boundary varies. Instead of equation (24), the bottom boundary condition was taken to be

$$J_{\nu 3/2} = S_{\nu 3/2} . \tag{27}$$

This makes the net heating in the bottom zone zero, which is approximately true at great depth in the atmosphere and does not affect the overall energetics of the atmosphere.

The dynamics boundary conditions were that the gas velocity at the bottom boundary equal the constant piston velocity and that the upper boundary be perfectly transmitting:

$$\frac{\partial u}{\partial t} = -s\frac{\partial u}{\partial R} , \tag{28}$$

where s is the sound speed.

d) Initial Model Atmosphere

The initial atmosphere was taken to be in radiative, hydrostatic, and statistical equilibrium, and its structure was found by solving equations (1)–(6) with the time-dependent terms set equal to zero. We specified a surface gravity of $g = 10^4$ and a Lyman continuum flux of $F/4\pi = 10^4$ ergs cm^{-2} s^{-1}. The model atmosphere is illustrated in Figure 1. The density scale height varies between 1.4 and 1.9 Mm. The surface gravity and temperature structure were chosen to illustrate interesting physical effects. They are similar to those of an A0 main-sequence star.

Our initial estimate for the temperature structure $T(\tau)$ of the static atmosphere was the exact solution for one angle and one frequency point. If $\mathcal{H} = F/4\pi$ is the net flux and τ is the optical depth, the radiative-equilibrium solution for the integral over the Lyman continuum of the Planck function is given by

$$B(\tau) = \frac{\mathcal{H}}{\mu}\left(1 + \frac{\tau}{\mu}\right) . \tag{29}$$

We approximated the frequency integral of the Planck function by the expression

$$B(\tau) = \int_{\nu_L}^{\infty} d\nu B_\nu(\tau) = \omega_1 \frac{2h{\nu_L}^3}{c^2}\frac{1}{\exp(h\nu_L/kT) - 1} , \tag{30}$$

where ω_1 is a suitably chosen weight factor. Thus the temperature distribution is given by

$$T(\tau) = \frac{h\nu_L}{k}\frac{1}{\ln\{1 + [1/\gamma(1 + \tau/\mu)]\}} , \tag{31}$$

where

$$\gamma = \frac{\mathcal{H}}{\mu}\frac{c^2}{2h{\nu_L}^3\omega_1} . \tag{32}$$

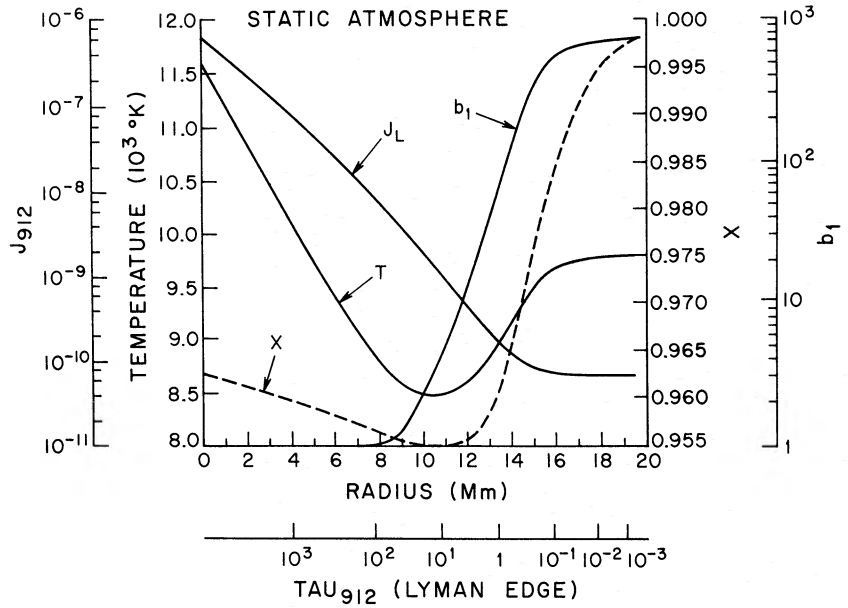

FIG. 1.—Static atmosphere: mean intensity of radiation at the Lyman edge (ergs cm^{-2} s^{-1} Hz^{-1}), temperature (10^3 K), degree of ionization (*dashed line*), and departure coefficient as functions of optical depth and height. The zero point for the height scale is the initial piston position at $\tau_L = 8000$.

For the initial temperature distribution (31), we calculated the corresponding populations and intensities of the radiation field. With these results as a starting solution, we determined the structure of the static atmosphere by solving the time-independent forms of equations (1)–(6) by Newton-Raphson iteration.

The most interesting feature of the static atmosphere is the temperature reversal due to departures from LTE in the Lyman continuum (Fig. 1) (Cayrel 1963; Kalkofen 1968). This effect follows from the constraints of flux conservation in the Lyman continuum and statistical equilibrium for a gas of one-level atoms whose density is low enough that its structure depends mainly on radiative transitions and is hardly influenced by collisions. The absorption coefficient in the Lyman continuum decreases with increasing frequency, and hence radiation near the Lyman edge comes from cooler surface layers and that at higher frequencies comes from deeper, hotter layers.

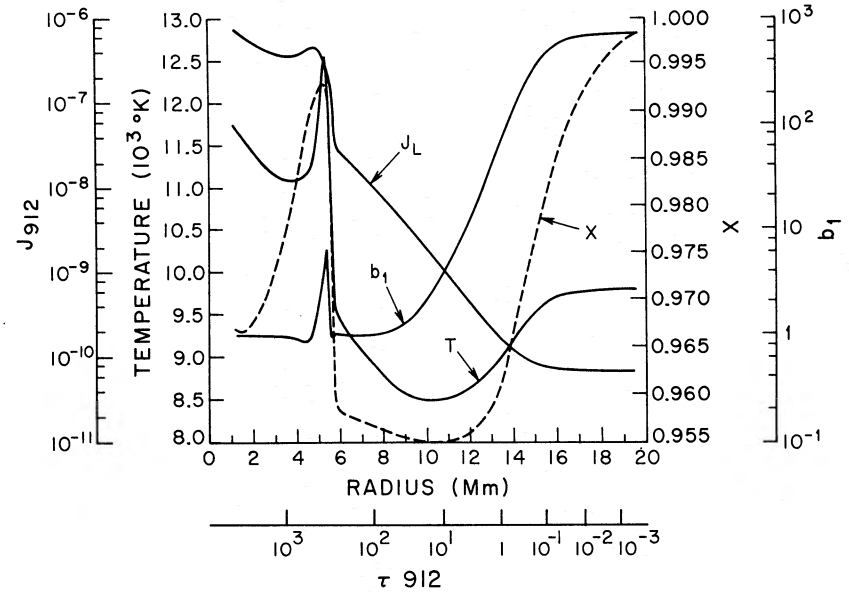

FIG. 2.—Shock before formation of I front; $\tau_{shock} = 360$. Lyman-edge radiation field, temperature, degree of ionization (*dashed line*), and departure coefficient as functions of height and optical depth.

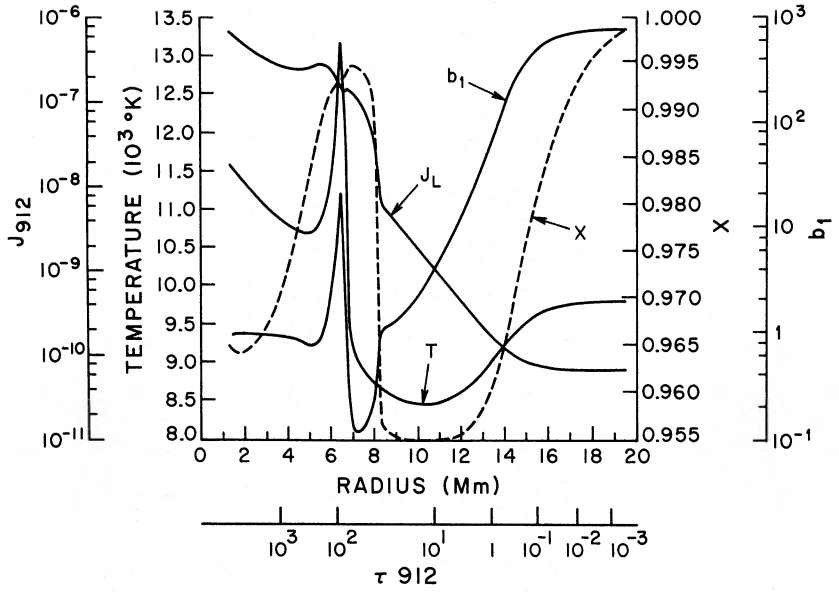

FIG. 3.—Shock ($\tau_{shock} = 83$), with I front propagating ahead. Lyman-edge radiation field, temperature, degree of ionization (*dashed line*), and departure coefficient as functions of height and optical depth.

Since the integrated flux is conserved, the intensity near the Lyman edge must be smaller—and at higher frequencies, larger—than the corresponding Planck function. Radiative transitions depend on photon density rather than on energy, so the weaker radiation field near the Lyman edge produces less ionization and therefore a larger ground-state population. This increases the energy absorption over emission until the kinetic temperature rises sufficiently to bring them into balance. We will explore this problem more fully in a forthcoming paper.

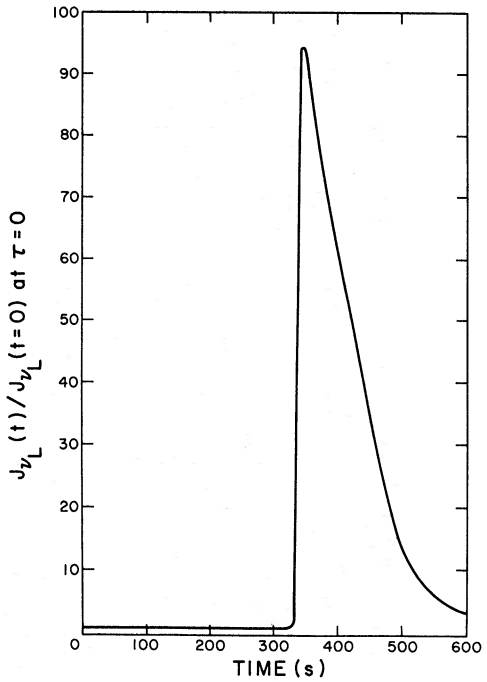

FIG. 4.—Surface luminosity flash. $J_{\nu_L}(t)/J_{\nu_L}(t = 0)$ at $\tau = 0$ versus time.

III. PISTON-DRIVEN SHOCK MOVING THROUGH A STATIC ATMOSPHERE

a) Description

The shock structure is determined by the radiative and collisional processes occurring in the shock wave and can be understood in terms of the corresponding relaxation lengths. The slowest process determines the time required to establish equilibrium behind the shock front.

When the shock is deep in the atmosphere (Fig. 2), the temperature at the shock shows a rapid rise to a sharp peak and then a fairly steep drop back to its equilibrium value. The temperature spike, when the shock front is at an optical depth of $\tau_{912} = 360$, has a width of approximately 650 km, corresponding to an optical thickness of $\Delta\tau_{912} \approx 70$. The intensity of the radiation field also has a sharp gradient at the shock front.

When the shock front is at an optical depth of approximately $\tau_{912} = 200$, an ionization front (I front) forms and moves out ahead of the shock (Fig. 3). The hot gas in the shock front emits photons that are absorbed by the neutral atoms in the preshock gas. This is a *photoionizing precursor* eating its way into the partially ionized gas ahead of the shock and depleting the neutral atoms. The radiation intensity at the Lyman edge builds up ahead of the shock in the precursor region. Within 50 s, during which the shock has traveled 1.3 Mm ($\tau_{912} = 17$), the photoionization precursor has ionized the entire atmosphere. The density of neutral atoms has been reduced by a factor of 100, which lowers the optical depth to the shock front to 17. This increases the radiation field by two orders of magnitude over its ambient value (Fig. 4). When the I front reaches the surface, it produces a luminosity flash with a rise time of less than 25 s and a decay time of the order of 100 s. Bopp and Moffett (1973) note the existence of a flash in the visible light of flare stars. It will thus be of interest to investigate whether the luminosity

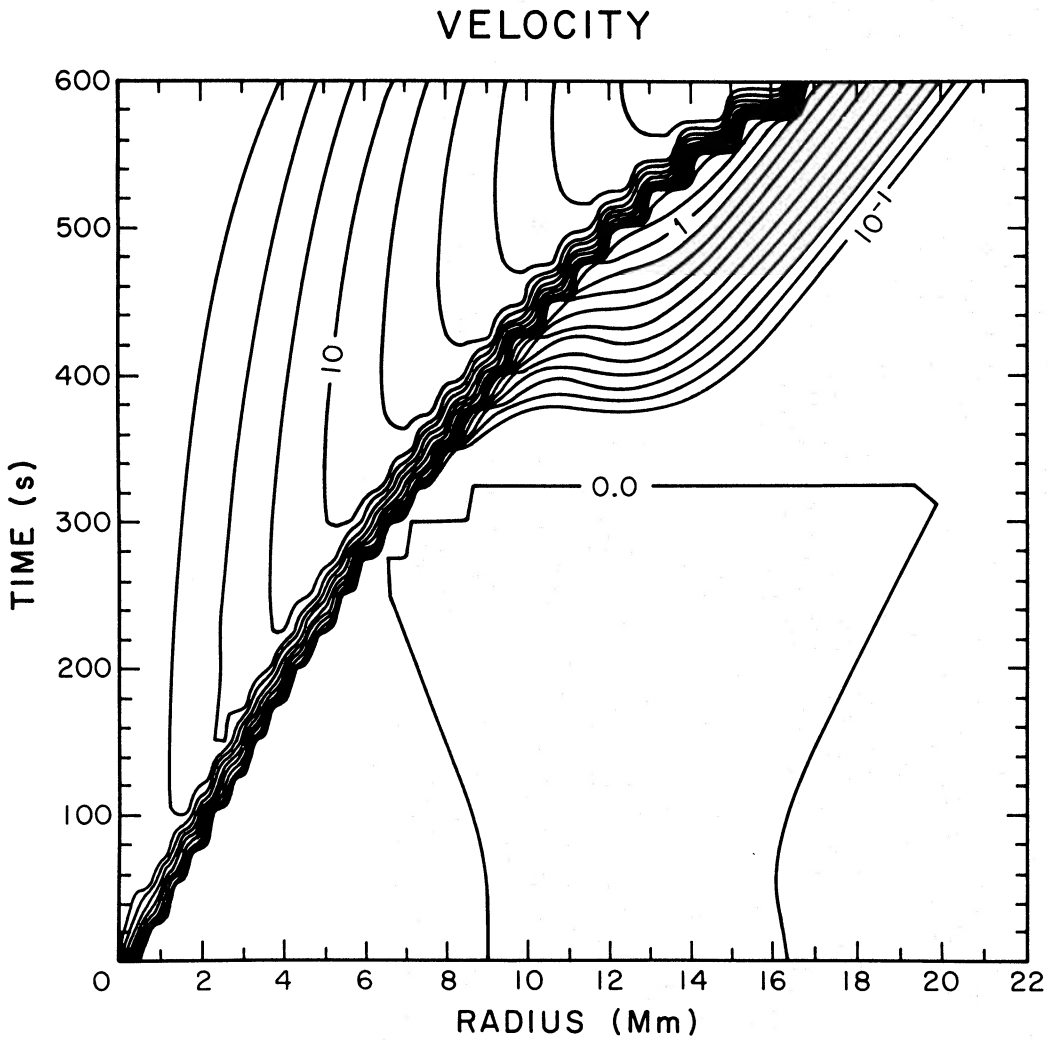

FIG. 5.—Fluid velocity (km s^{-1}). Contour interval is $\Delta \log V = 0.1$.

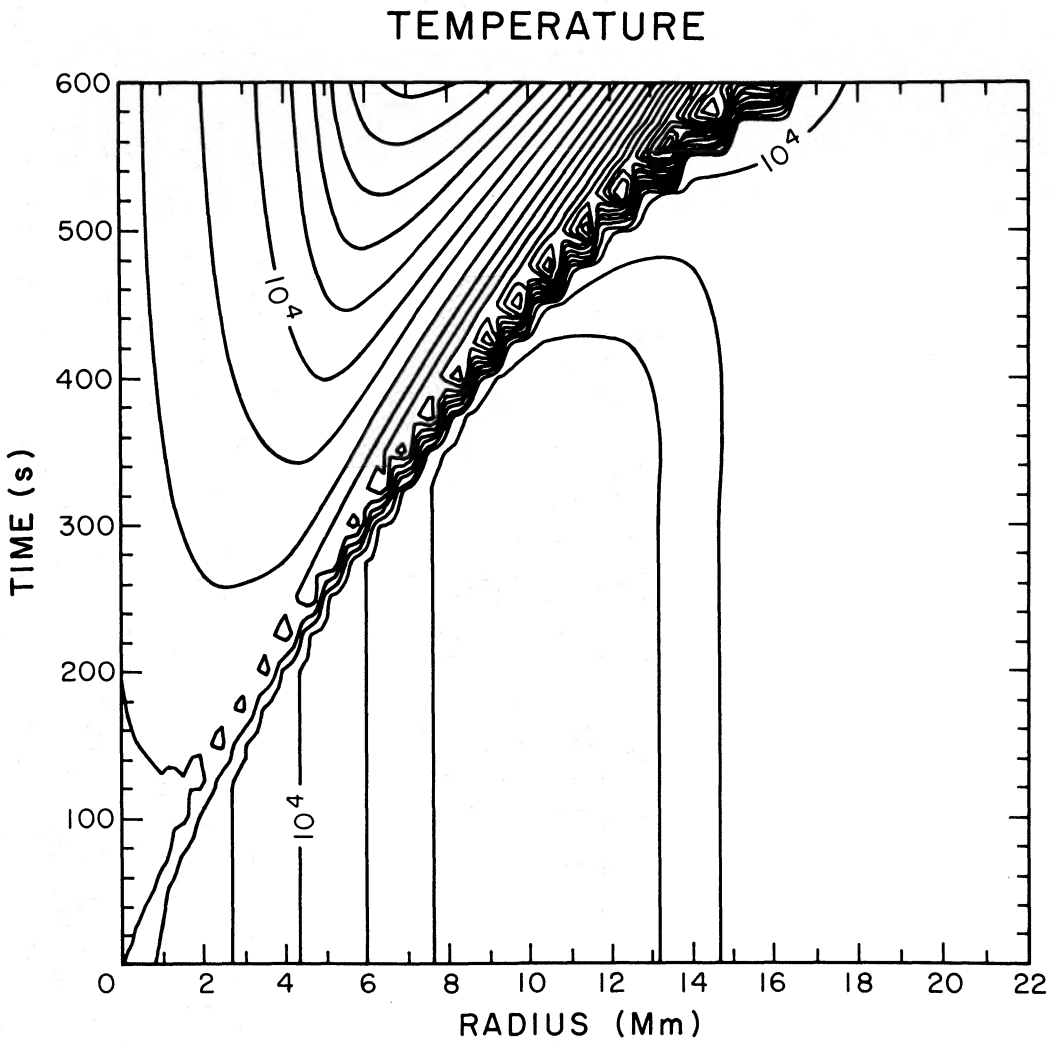

FIG. 6.—Temperature (K). Contour interval is $\Delta \log T = 0.03$.

flash we found persists when higher continua are included. If so, the photoionization precursor could suggest a possible flare mechanism.

The propagation of the shock wave and ionization front are displayed in contour maps of velocity, temperature, degree of ionization, and intensity of the radiation field (Figs. 5–8). The shock is recognizable by the crowding of the contour lines. Before the ionization front forms, the shock is visible in the contour plots of all the variables; after it forms, the shock is visible primarily in the velocity and temperature contours. The ionization front breaks away from the shock, reaching the outer limits of the atmosphere between 300 and 350 s. The shock, lagging far behind the precursor, continues moving upward. Note that the pressure in the preshock gas is increasing because of energy absorbed from the precursor radiation. This increased pressure accelerates the gas to velocities of the order of 1 km s^{-1} (Fig. 5).

Let us next focus our attention on the ionization contour (Fig. 7). Deep in the atmosphere, the degree of ionization decreases rapidly behind the shock. As the shock moves outward, the ionization drop behind the front becomes more gradual. The ionization returns part way to its equilibrium value, but then remains nearly constant in a continually widening plateau. It finally returns to its equilibrium value at an ever lengthening distance behind the shock front. This ionization plateau will be seen to result from the slow collisional recombination rate in region III.

When the shock has passed through most of the atmosphere, its prominent features are a sharp increase in temperature at the shock front and a rapid drop in temperature with a corresponding fall in ionization, just behind the shock front (region I) (Fig. 9). Note that the temperature spike is narrower than at earlier times. Behind the temperature spike, the degree of ionization remains almost constant for a distance of approximately 4 Mm (region II) and then begins to fall rapidly (region III). The radiation field at the Lyman edge J_{ν_1} exhibits a plateau in the region of rapid drop in ionization.

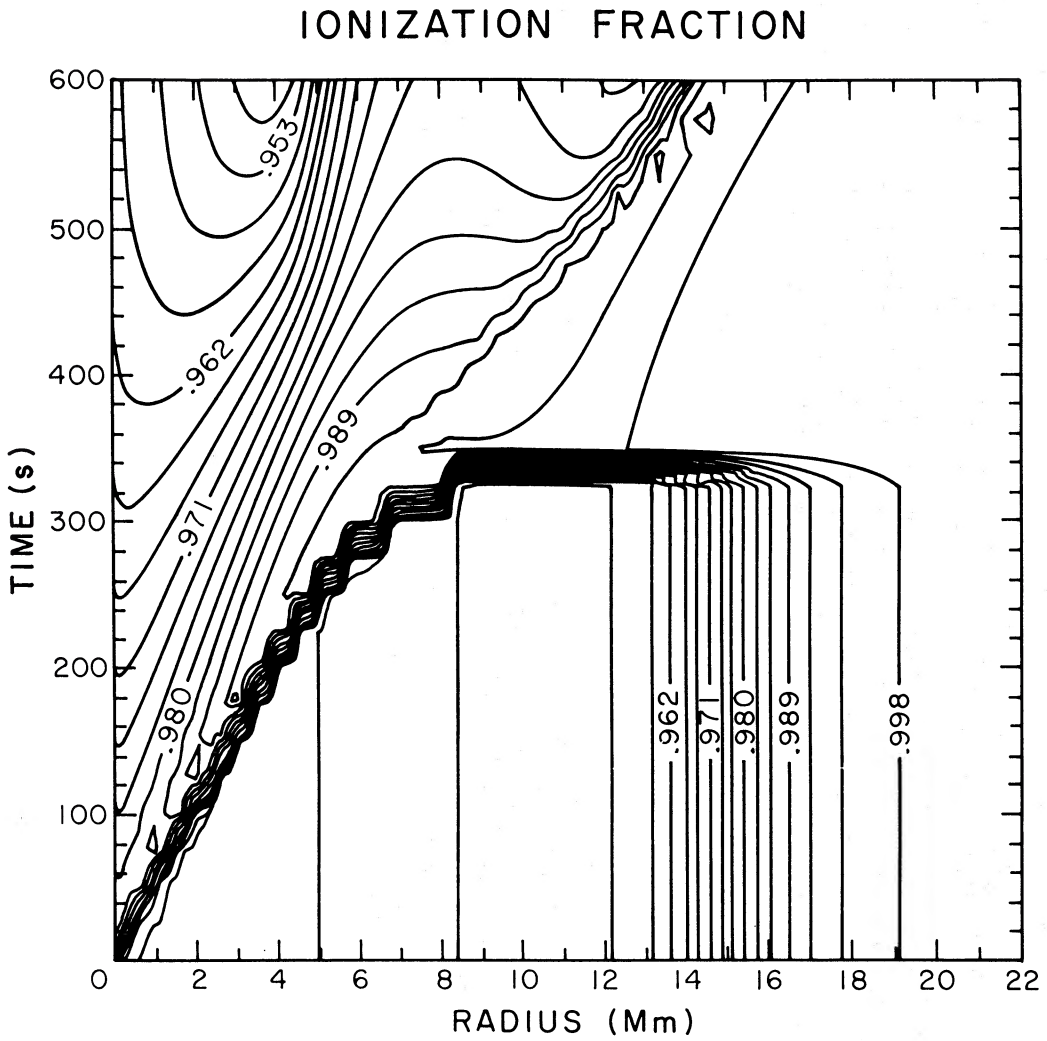

FIG. 7.—Degree of ionization. Contour interval is $\Delta X = 0.003$.

We have described the shock structure in terms of several different regions. The shock front is an *external relaxation region*, where elastic collisions convert directed motion into random motion. In order to brake the fast incoming particles in the shock front, several elastic collisions are required. The relaxation of the translational degrees of freedom occurs over distances of the order of a collisional mean free path. We did not treat the gas from a kinetic point of view, and this so-called external relaxation region is spread over three to four mesh zones by the artificial viscosity. Behind the shock front is an *internal relaxation region*, where radiative transitions and inelastic collisions distribute some of the energy of random motion over various internal degrees of freedom, such as ionization. Radiation emitted in the Lyman continuum behind the shock propagates through the shock into the partially ionized preshock gas. Therefore, the preshock region is influenced by conditions in the postshock relaxation region.

As the shock wave moves through the atmosphere, the collisional and radiative time scales and their corresponding lengths in the postshock region change in relative importance in determining the postshock structure. In order to compute representative length scales from the time scales, we chose as a characteristic velocity the difference $(V_s - V_p)$, where V_s is the shock velocity and V_p is the maximum fluid velocity at a specific time. The photon mean free path, the length scales for radiative recombination, collisional recombination, collisional ionization, and photoionization are as follows:

$$\lambda_\gamma = \frac{1}{n_1 \sigma(\nu)}, \qquad \lambda_{\text{rad-rec}} = \frac{(V_s - V_p) n_e}{n_1^* R_{K1}'},$$

$$\lambda_{\text{coll-rec}} = \frac{(V_s - V_p) n_e}{n_1^* C_{1K}}, \qquad \lambda_{\text{coll-ion}} = \frac{V_s - V_p}{C_{1K}},$$

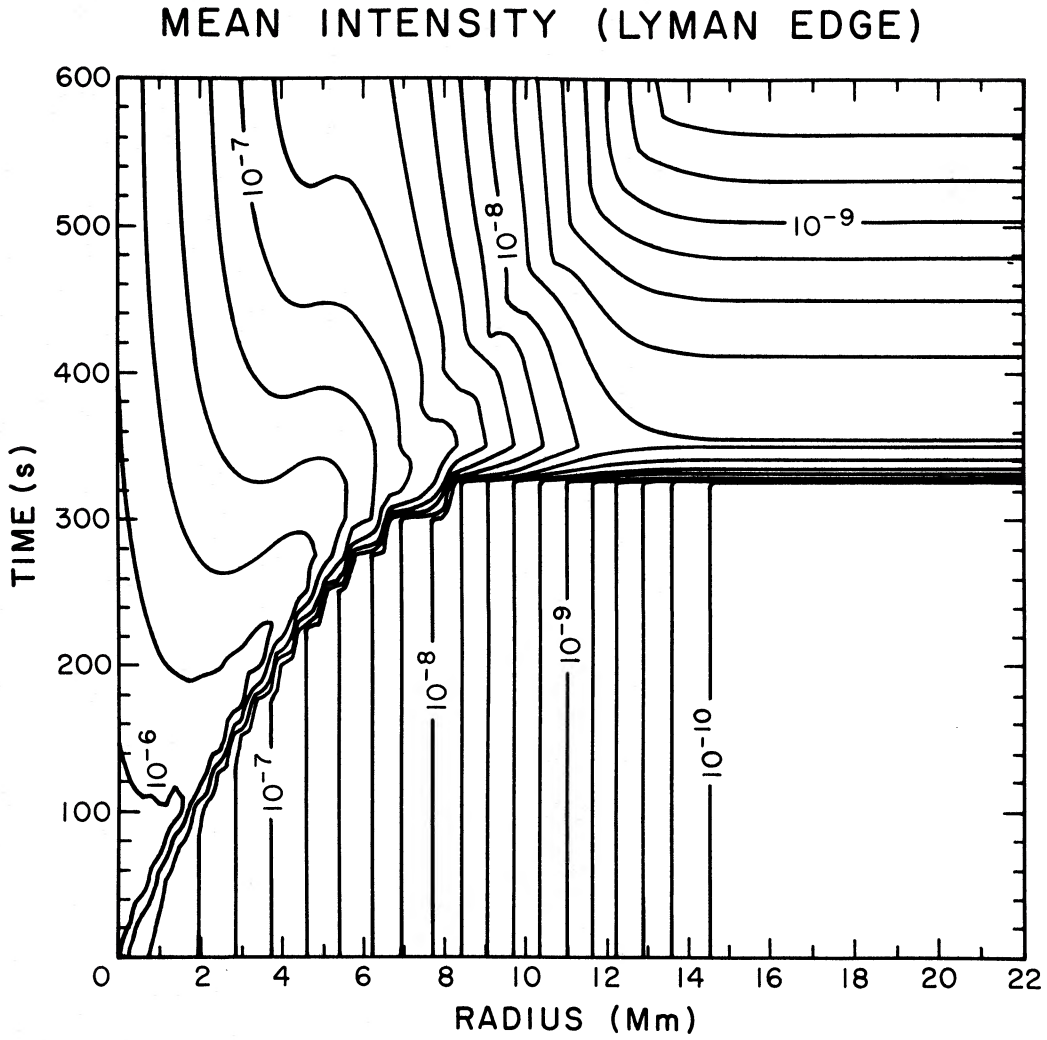

FIG. 8.—Radiation intensity at the Lyman edge (ergs cm^{-2} s^{-1} Hz^{-1}). Contour interval is $\Delta \log J = 0.2$.

TABLE 1

CHARACTERISTIC LENGTHS

Comment	t (s)	Z (shock front) (Mm)	$\lambda\gamma$ (km)	$\lambda_{\text{rad-ion}}$ (km)	$\lambda_{\text{rad-rec}}$ (km)	$\lambda_{\text{coll-ion}}$ (km)	$\lambda_{\text{coll-rec}}$ (km)
Deep	126	2.8	1.34	0.0129	1.047	19.7	1.45×10^3
	201	4.2	4.33	0.018	2.04	262	4.99×10^4
Before formation of I front	251	5.3	8.7	0.0265	3.57	625	2.83×10^5
Slight precursor	300	6.6	17.6	0.0457	6.39	730	6.87×10^5
Full I front	325	7.2	26	0.062	8.47	1.09×10^3	1.31×10^6
Just after I front	350	8.0	35	0.0947	12.2	1.06×10^3	2.58×10^6
	400	9.0	62.5	0.272	27.6	135	1.76×10^6
Shallow	450	10.4	121	1.02	78.2	80	1.58×10^7
	525	13.5	975	7.44	405	61	2.52×10^8
	575	16.0	3.1×10^3	4.29	2.0×10^3	32.7	6.0×10^{10}

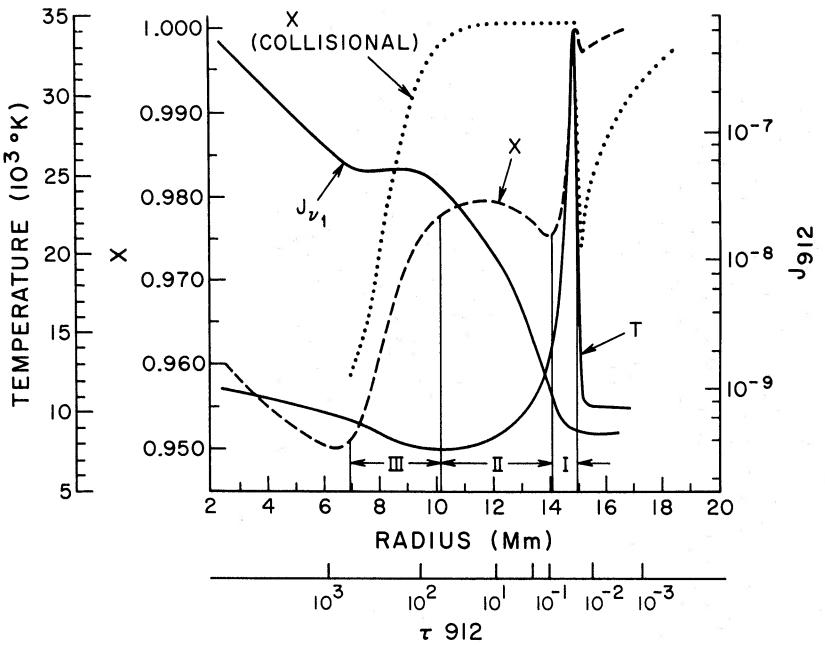

FIG. 9.—Shock in upper atmosphere ($\tau_{\text{shock}} = 0.034$). Lyman-edge radiation field, temperature, ionization (radiation case, *dashed line*), and ionization (collisional case, *dotted line*) as functions of height and optical depth.

and

$$\lambda_{\text{rad-ion}} = (V_s - V_p)/R_{1K} .$$

Table 1 gives values of the length scales for several stages in the propagation of the shock through the atmosphere. These length scales are computed at the point of maximum fluid velocity except for $\lambda_{\text{coll-ion}}$, which was evaluated at a point slightly in front of the peak velocity. Their values are uncertain by factors of 2 or 3, depending on the position in the shock where they are computed.

b) Temperature Spike

Deep in the atmosphere the structure of the shock wave is determined predominantly by collisional processes. The most pronounced feature of the shock structure is the temperature spike.

It is useful to compare the structure of the temperature spike obtained by numerical calculation for the three cases: (1) adiabatic shock, (2) collisional shock (no radiative transitions), and (3) radiating shock (both radiative and collisional transitions) (Table 2). A comparison of Tables 1 and 2 shows that deep in the atmosphere, when $Z_{\text{shock}} \lesssim 7$ Mm, the collisional ionization length $\lambda_{\text{coll-ion}}$ is in excellent agreement with the width of the temperature spike, and the width for the radiating shock is the same as that for a shock where only collisional transitions occur. This indicates that collisional losses of the electron gas account for most of the drop in temperature from its peak at the shock front to a distance of 0.1–0.5 Mm, approximately $\lambda_{\text{coll-ion}}$, downstream.

TABLE 2

TEMPERATURE SPIKES

Case	Height* (Mm)	Width at Half-Maximum (Mm)
Radiating.....	7.1	0.5
Collisional.....	7.0	0.5
Adiabatic.....	7.5	0.75
Radiating.....	10.6	0.5
Collisional.....	10.8	0.56
Adiabatic.....	10.1	0.67
Radiating.....	13.8	0.31
Collisional.....	14.5	0.64
Adiabatic.....	13.9	0.67

* The zero point for the height scale is the initial piston position at $\tau_{912} = 8000$.

Radiation plays only a small role in the structure of the shock deep in the atmosphere because radiative ionizations and recombinations balance each other over very short distances. The energy-loss process is a cycle of collisional ionization followed by radiative recombination. Each ionization results in the electron gas losing an amount of thermal energy equal to $\chi_H = 13.6$ eV. The temperature of the electron gas is on the order of 10^4 K ≈ 1 eV. Thus, the formation of a new electron requires an energy equal to the thermal energy of approximately 13 electrons. The energy loss of the electrons is reflected in the temperature drop of the gas.

To investigate the effectiveness of radiation in cooling the shock to form the spike, we computed the ratio of the net radiative cooling in the tail of the shock to the energy convected into the shock front,

$$\int \mathscr{H} dx/(\tfrac{1}{2}\rho V^3),$$

where

$$\mathscr{H} = 4\pi \int_{\nu_L}^{\infty} (\chi_\nu J_\nu - \eta_\nu) d\nu$$

is the divergence of the radiative flux.

We considered the case when the shock was at an optical depth of 83. By using the trapezoidal rule, the integral was evaluated from the peak of the temperature spike back into the shock a distance of 1 Mm or $\Delta\tau \approx 35$, which spans five mass zones in our spatial grid. Farther back, the flux divergence was insignificant. The density ρ and velocity V were evaluated at a point slightly in front of the shock front. We found

$$\int \mathscr{H} dx \approx 6.7 \times 10^5 \text{ ergs cm}^{-2} \text{ s}^{-1},$$

$$\tfrac{1}{2}\rho V^3 = 6.0 \times 10^6 \text{ ergs cm}^{-2} \text{ s}^{-1}.$$

Thus, when the shock is deep in the atmosphere, radiative cooling in the postshock region amounts to only 10 percent of the energy flux convected into the shock. When radiation cannot escape, it is not effective in removing energy from the gas behind the shock front.

The adiabatic shock is seen to have a larger width than do either the radiating or the collisional shocks, because expansion is the only process available for cooling in this case, while the radiating and collisional shocks have collisional ionization as an additional mechanism.

The postshock conditions can be compared with those of a *steady shock* (Zel'dovich and Raizer 1967). The effects of ionization on the gas structure are included in the Rankine-Hugoniot relations through the Saha equation. The energy equation with ionization is

$$\frac{\gamma}{\gamma - 1}\frac{P_1}{\rho_1} + \tfrac{1}{2}V_1^2 = \frac{\gamma}{\gamma - 1}\frac{P_2}{\rho_2} + \tfrac{1}{2}V_2^2 + Q, \tag{33}$$

where $Q = (x_2 - x_1)(\chi_H/m_H)$ is the ionization energy per unit mass that the postshock gas must supply in ionizing hydrogen. (Subscripts 1 and 2 refer to upstream and downstream conditions, respectively.) The degree of ionization, $x = n_e/(n_1 + n_e)$, can be expressed in terms of the temperature and density by means of the Saha equation. The energy equation (33), combined with the mass conservation equation $\rho_1 V_1 = \rho_2 V_2$, gives

$$\frac{\rho_2}{\rho_1} = \frac{P_1(\gamma - 1) + P_2(\gamma + 1)}{P_1(\gamma + 1) + P_2(\gamma - 1)} + \frac{2Q(\gamma - 1)\rho_2}{P_1(\gamma + 1) + P_2(\gamma - 1)}, \tag{34}$$

which can be rewritten, by use of the equation of state $P = \rho RT(1 + x)$, as

$$\rho_2^2 RT_2(1 + x_2)(\gamma - 1) + \rho_2[P_1(\gamma + 1) - \rho_1 RT_2(1 + x_2)(\gamma + 1) - 2Q\rho_1(\gamma - 1)] - \rho_1 P_1(\gamma - 1) = 0. \tag{35}$$

The velocity change across the shock is

$$U \equiv V_1 - V_2 = [(P_2 - P_1)(V_1 - V_2)]^{1/2}.$$

We combined this expression for the velocity U with equation (34) to solve for the pressure ratio (P_2/P_1):

$$\frac{\rho_2}{P_1} RT_2(1 + x_2) - 1 - \frac{\gamma(\gamma + 1)U^2}{4C_1^2} + \frac{Q(\gamma - 1)\rho_1}{2P_1} - \frac{\gamma U}{C_1}\left[1 + \frac{(\gamma + 1)^2}{16C_1^2}U^2 - \frac{Q(\gamma - 1)(\gamma + 1)}{4\gamma}\frac{\rho_1}{P_1} + Q^2(\gamma - 1)^2\left(\frac{\rho_1 C_1}{4P_1 U\gamma}\right)^{1/2}\right]^{1/2} = 0. \tag{36}$$

The nonlinear equations (35) and (36) were solved by a Newton-Raphson iteration for the postshock density and temperature, T_2, with a first guess taken from the solution of the Rankine-Hugoniot equations without ionization

(the steady adiabatic solution), $T_{2(AD)}$. The parameters were similar to those of our model at $t = 350$ s. We used a piston velocity $U = 10$ km s^{-1} corresponding to the fluid velocity behind the shock, $T_1 \approx 9000$ K, $\rho_1 \approx 10^{-11}$ g, and $x_1 = 94$ percent. Solution of equations (35) and (36) gives a downstream temperature $T_2 = 1.18 \times 10^4$ K. The steady-state adiabatic calculation gives $T_{2(AD)} = 1.48 \times 10^4$ K. The time-dependent calculation yields a downstream temperature $T_2 = 1.05 \times 10^4$ and $T_{peak} = 1.35 \times 10^4$. Thus, the amount of energy spent in collisional ionization corresponds to a temperature drop of 3000 K, in agreement with the drop obtained from the steady-state calculation.

In conclusion, when the shock is deep in the atmosphere, its temperature peak and relaxation can be interpreted as due to a weakly radiating shock whose structure is controlled by collisional ionization.

As the shock propagates up through the atmosphere, radiation plays an ever increasing role in determining the temperature spike. High in the atmosphere, the optically thin postshock gas is rapidly cooled by collisional ionization, followed by radiative recombination. The neutral atoms produced by radiative recombinations are reionized by electron collisions, which use up a large amount of thermal energy. The electrons and ions then recombine to emit photons that can escape from the postshock region and remove the ionization energy. The radiative relaxation length is larger than the collisional ionization length at heights above 10 Mm, and it now determines the structure of the temperature spike.

The loss of recombination radiation accounts for a large part of the rapid cooling and drop in ionization in region I for the case of the radiating shock. The integral of the flux divergence $\mathscr{H}$ from the peak of the shock front through region I when $\tau_{shock} = 0.38$, evaluated as previously, is

$$\int \mathscr{H} dx \approx 3.17 \times 10^4 \text{ ergs cm}^{-2} \text{ s}^{-1} .$$

This flux is comparable to the energy convected *into* the shock front, $\frac{1}{2}\rho V^3 = 4.9 \times 10^4$ ergs cm^{-2} s^{-1}. Thus, 65 percent of the energy flowing in the shock is being radiated away in region I. Recall that when the shock is deep in the atmosphere ($\tau_{shock} = 200$), only 10 percent of the inflowing energy is radiated away. The shock has now become strongly radiation-dominated, a consequence of the greatly reduced opacity of the upper part of the atmosphere.

When the shock is at about 14.0 Mm ($\tau_{shock} \approx 0.13$), the radiating shock is much narrower (Table 2, Fig. 10) than the collisional shock, because now radiative losses are an additional mechanism for shock cooling. The collisional shock in turn remains narrower than the adiabatic shock, because collisional ionizations provide a cooling mechanism in addition to the cooling by expansion. Collisional ionization, which becomes significant just at the shock front, produces a small jump in the ionization at the shock front in the radiation case (Fig. 9). The collisional ionization rate here is large despite the low electron densities. Recall that the collisional ionization

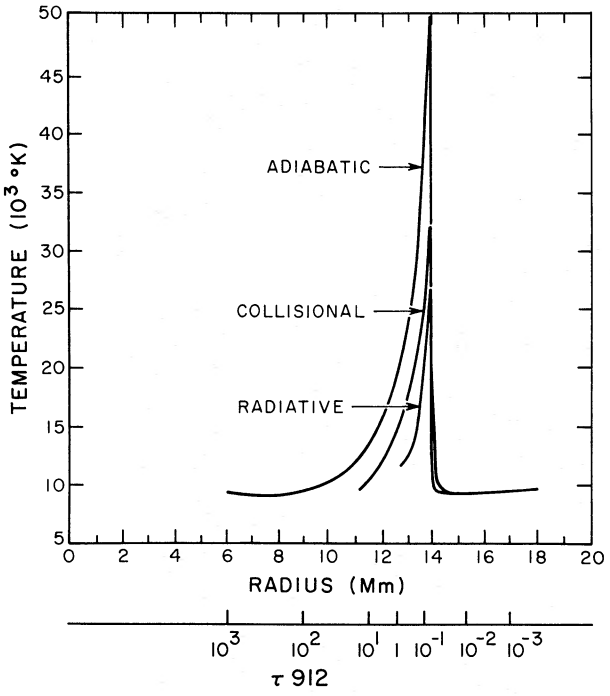

FIG. 10.—Comparison of temperature spikes for adiabatic, collisional, and radiative cases, for shocks at $\tau_L = 0.21$

frequency C_{1K}, which is proportional to $n_e T^{1/2} \exp(-h\nu/kT)$, depends exponentially on local temperature, which is high, $T \approx 3.5 \times 10^4$ K. Thus, C_{1K} exceeds the radiative ionization frequency R_{1K} at the shock front.

We note parenthetically that the artificial viscosity may have an important effect on departures from LTE in the shock front. For example, when the ionization front forms, the departure coefficient b_1 in the shock front has increased to a value of 10. If we write $b_1 = n_1\phi(T)/n_e^2$, where $\phi(T) \propto T^{3/2} \exp(-h\nu/kT)$ is the temperature factor from the Saha equation, we see that changes in b_1 can be predicted on the basis of instantaneous changes in the gas density and temperature brought about by an infinitesimally thin shock. Given the density and temperature change that a mass element in the shock front experiences at this time, $b_1 \approx 35$ would be predicted. Instead, the numerical solution of the equations gives $b_1 \approx 10$. This discrepancy can be understood as a consequence of the artificial viscosity spreading the shock over three or four zones. Hence, a particle entering the shock front does not experience instant changes in ρ and T but must go through a finite shock thickness. During the time the gas takes to pass through the dispersed shock, finite collisional and radiative rates have time to readjust n_1 and n_e partially to the changed local conditions and hence reduce b_1 in the peak. This is a very real effect, brought about by the artificial viscosity. The artificial viscosity can be reduced, however, because radiation provides some of the necessary smoothing.

Cannon (1974*a*, *b*) has solved the coupled fluid-dynamic and radiative-transfer equations by means of a perturbation expansion technique. His method depends on the assumption that the flux divergence $\mathscr{H}$ is small in comparison to the other terms appearing in the energy equation and can be regarded as a first-order perturbation on the system. He has considered two problems, a spectral line and a continuum, both for a two-level atom. While his assumption may be plausible for some spectral lines, the continuum-radiation flux divergence will, in general, be comparable to the other terms in the energy equation near optical depth unity. In our case, 65 percent of the energy convected into the shock in optically thin regions is radiated away. This suggests that a perturbation expansion in $\mathscr{H}$ should fail. The adiabatic solution may be so significantly different (Fig. 10) from the radiation case that it cannot be used as the first term in a perturbation expansion, as Cannon does.

c) Ionization Front

An outward-propagating photoionization precursor or I front moves ahead of the shock when the shock is at $\tau_{912} = 200$ ($t = 300$ s) and reaches the surface by $t = 350$ s (Fig. 3). Its properties can be compared with those of a quasi-steady ionization front. We solved the steady-flow equations for the velocity of the I front, using parameters from our model, and compared the result with the actual value obtained in the time-dependent calculation. We also examined the critical conditions necessary for an I front to propagate outward and checked to see that these critical conditions were satisfied where we observed the I front.

The velocity of the ionization front is found from the condition that the flux of hydrogen atoms through the front equals the flux of ionizing quanta falling on the surface of the front per unit time, because each hydrogen atom that crosses the I front must be ionized by a photon. Thus,

$$n_1 V_1 = N_{\rm LC}\,, \tag{37}$$

where n_1 is the density of neutral hydrogen atoms, V_1 is the velocity of the ionization front, and $N_{\rm LC}$ is equal to the number of Lyman continuum photons passing per unit area and unit time through the front:

$$N_{\rm LC} = \int dx \int d\nu(\mathscr{H}_\nu/h\nu) \approx (1/h\nu_{\rm L}) \int dx \mathscr{H}\,.$$

The parameters of our model at $t = 300$ s are

$$n_1 = 3.3 \times 10^{10}\ {\rm cm}^{-3}\,, \qquad T_1 = 8500\ {\rm K}\,,$$

$$N_{\rm LC} \approx 8 \times 10^{16}\ {\rm photons\ cm}^{-2}\ {\rm s}^{-1}\,.$$

Therefore,

$$V_1 = \frac{N_{\rm LC}}{n_1} = \frac{8 \times 10^{16}}{3.3 \times 10^{10}} \approx 25\ {\rm km\ s}^{-1}\,.$$

The I-front velocity computed from the time-dependent calculation between 300 and 325 s is $V_1 \approx 30$ km s^{-1}. Thus, the quasi-steady model provides a good interpretation of the velocity of the ionization front in the nonsteady situation.

Kahn (1954) determined the conditions the gas must satisfy at the surface (I front) separating the partially ionized region of the atmosphere from the fully ionized region. He showed that an I front will advance supersonically into the undisturbed region if its speed V is larger than the critical speed V_R and if its photon flux Φ is larger than the critical flux Φ_R, where $V_R = \frac{1}{2}[2Q + (4Q^2 + 9C^2)^{1/2}]$, $\Phi_R = n_1 V_R$, $Q^2 = 2kT/m_{\rm H}$, and $C^2 = \gamma RT_1/\mu_1$. If these conditions are satisfied, the motion is also supersonic with respect to the gas behind the I front, provided the

density change across the front is small. This condition is referred to as weak *R*-type. Using the parameters of our model—$T_1 = 8.5 \times 10^3$ K and a mean molecular weight of $\mu_1 \approx 0.5$—we obtained

$$Q^2 = \frac{2kT}{m_H} = 1.35 \times 10^{12} \text{ cm}^2 \text{ s}^{-2}$$

and

$$C^2 = \frac{\gamma RT_1}{\mu_1} = 2.36 \times 10^{12} \text{ cm}^2 \text{ s}^{-2} .$$

With these values, the critical conditions for the existence of an *R*-type front are

$$V_R = 22.4 \text{ km s}^{-1}$$

and

$$\Phi_R = 8.0 \times 10^{16} \text{ photons cm}^{-2} \text{ s}^{-1} .$$

The photon flux is nearly constant, but n_1 decreases exponentially. The I-front velocity N_{LC}/n_1 thus increases as it moves through the atmosphere. At $t = 300$ s, the critical conditions for an *R-type* (weak) I front are just satisfied. The I front then moves rapidly away from the shock front and totally photoionizes the entire atmosphere within an interval of about 50 s.

d) Constant Ionization Plateau

When the shock is far out in the atmosphere (Fig. 9), the rapid cooling by radiative recombination, region I, is followed by a large region of almost constant ionization, region II.

The important cooling processes in this region were found by evaluating the different terms in the energy equation (15). For example, at 550 and 575 s, the variables in the energy equation toward the front of region II are

$$t = 550 , \qquad t = 575 ,$$

$$\tau_{912} = 0.96 , \qquad \tau_{912} = 1.36 ,$$

$$V^n = \frac{1}{\rho^n} = 2.86 \times 10^{12} , \qquad V^{n+1} = 3.38 \times 10^{12} ,$$

$$P^n = 0.8755 , \qquad P^{n+1} = 0.6326 ,$$

$$\mathscr{H}^n = -4.655 \times 10^{-4} , \qquad \mathscr{H}^{n+1} = -8.257 \times 10^{-5} ,$$

$$n_e{}^n = 2.046 \times 10^{11} , \qquad n_e{}^{n+1} = 1.727 \times 10^{11} .$$

Thus the terms in the energy equation become

$$P\Delta V = 3.92 \times 10^{11} ,$$

$$I^{n+1} - I^n = \chi_H \left(\frac{n_e{}^{n+1}}{\rho^{n+1}} - \frac{n_e{}^n}{\rho^n} \right) = -2.18 \times 10^{10} ,$$

$$\frac{\Delta t 4\pi}{\rho^{n+1} + \rho^n} (H^{n+1} + H^n) = -2.66 \times 10^{11} .$$

Adiabatic expansion accounts for 60 percent of the cooling, while radiative emission accounts for 40 percent. Adiabatic expansion and radiative losses are thus about equally effective in cooling the gas in region II.

The size of the constant-ionization plateau (region II) is determined by the collisional recombination time. The ionization profiles for the collisional and radiative cases are compared in Figure 9. In the collisional case, the initial jump in ionization at the shock front is much larger because the preshock gas has not been ionized by a photoionization precursor, since no radiation is taken into account. The gas is ionized by collisions at the shock front and, once ionized, does not recombine rapidly, as it does in the radiation case, because radiative recombinations are excluded. The ionization in the collisional case stays constant over the same region in which the radiative case has a plateau. The collisional recombination time $t_{\text{coll-rec}} \approx (n_e/n_1{}^* C_{1K})$ remains longer than the gas travel time for a great distance behind the shock, so the gas does not have sufficient time to recombine. As we move to a greater distance behind the shock, where the density is higher, collisional recombination drives the gas back to equilibrium since $t_{\text{rad-rec}}/t_{\text{coll-rec}} \approx n_e$. In both the collisional and the radiative case, collisional recombination begins to become significant at the same depth, and so the constant ionization regions are of equivalent width (Fig. 9).

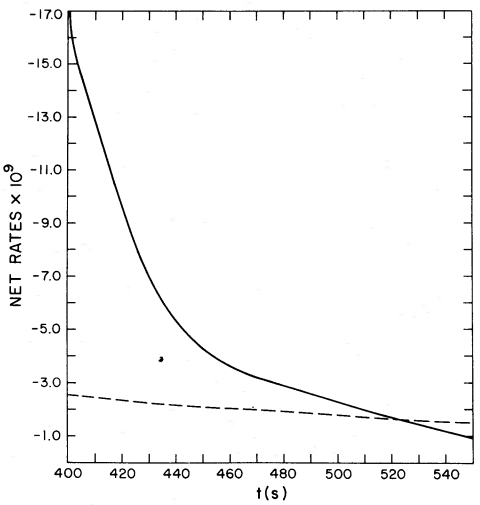

FIG. 11.—Net rates of radiative and collisional ionization in region III. Dashed line is $(n_1 R_{1K} - n_1^* R_{K1}')$; dotted line is $(n_1 C_{1K} - n_1^* C_{1K})$.

The constant-ionization plateau is bounded at the back by a recombination zone (region III) in which the gas finally relaxes back to its initial state. A plot of the net rates for a specified mass zone in this region (Fig. 11) reveals that radiative recombination dominates collisional recombination until $t = 530$ s, at which time three-body recombinations dominate and drive the gas to final equilibrium.

Note the existence of a shoulder or plateau in the mean intensity (at the Lyman edge) in region III (Figs. 8 and 9). This plateau is caused by the enhancement in the radiation field produced by the shock before the formation of the ionization front allowed the radiation to escape to the surface. After the shock passes, the radiation field slowly relaxes to equilibrium as photons diffuse into optically thinner regions of the gas. Eventually, we would expect the shoulder to relax completely.

We are indebted to Dimitri Mihalas and Lawrence Auer for helpful discussions. The timely help of Jordan Hastings of the National Center for Atmospheric Research (NCAR) in designing the contour plotting routines aided our understanding of the phenomena. We are grateful to Charles A. Whitney for a critical reading of the manuscript. R. I. Klein would like to thank the Smithsonian Astrophysical Observatory for support under a predoctoral Research Associateship for the duration of this research. The computations were performed at NCAR, which is sponsored by the National Science Foundation (NSF). This work was supported in part by NSF grant GP-42928.

APPENDIX

Two basic approximations in the calculations are (1) the neglect of the time-derivative term in the equations of radiative transfer and (2) the use of a single kinetic temperature for the electrons, ions, and atoms. We examine the validity of these approximations.

The transfer equation, including the time rate of change of the specific intensity, can be written

$$\frac{1}{c}\frac{dI_\nu}{dt} + \mu\frac{dI_\nu}{dz} = \eta_\nu - \chi_\nu I_\nu .$$

The contribution of far sources to the total intensity at a given point z in an absorbing medium decreases exponentially with distance. Photons that arrive at z are emitted at distances a few mean free paths $\lambda = 1/\chi_\nu$ away. Photons emitted at greater distances are absorbed before they reach z. Light travels a mean free path λ in a time $\tau_F = \lambda/c = 1/\chi_\nu c$. The time-dependent term in the transfer equation can be neglected if this photon travel time is much shorter than the characteristic time to produce a significant change in the state of the system. If this is not the case, the time of flight of the photon might make an important contribution to the transfer equation.

The thermal relaxation time, i.e., the characteristic time for a heated gas element to lose its energy by radiating it away, is the ratio of the internal energy per unit volume,

$$E = \tfrac{3}{2}NkT ,$$

to the emission rate per unit volume of the gas,

$$\epsilon = -4\pi \int_{\nu_L}^{\infty} \eta_\nu d\nu .$$

Here, η_ν is the emissivity, which can be expressed as

$$\eta_\nu = n_1^* \sigma_{1K}(\nu) \frac{2h\nu^3}{c^2} \exp(-h\nu_L/kT) ,$$

where

$$\sigma_{1K}(\nu) = \sigma_0/\nu^3$$

is the photoionization cross section and $\sigma_0 = 2.815 \times 10^{29}$. Hence,

$$\epsilon = -\frac{8\pi n_1^*}{c^2} \sigma_0 kT \exp(-h\nu_L/kT) .$$

Thus, the thermal relaxation time is

$$\tau_{th} \sim \left| \frac{E}{\epsilon} \right| = \frac{3c^2 N}{16\pi n_1^* \sigma_0 \exp(-h\nu/kT)} .$$

The ratio of the thermal relaxation time to the photon time of flight is

$$\frac{\tau_{th}}{\tau_F} = \frac{3}{16\pi} b_1 N \lambda_L^3 \exp(h\nu_L/kT) = 4.53 \times 10^{-17} N b_1 \exp(h\nu_L/kT) ,$$

where N is the total number density of the gas, λ_L is the wavelength at the Lyman limit, and b_1 is the departure coefficient of the hydrogen ground state. It appears that for a hot gas with interparticle spacing larger than the photon wavelength, the time-of-flight term may become important.

We evaluate τ_{th}/τ_F for our model at three positions: (1) near the bottom of the atmosphere, (2) inside the shock when it has propagated into very thin regions of the atmosphere and has heated the gas significantly, and (3) at the surface of the atmosphere, where the gas is extremely tenuous. Using typical values of N, T, and b computed from our model, we get the results in Table 3. It is clear that the thermal relaxation time is long compared with the photon time of flight throughout the atmosphere. We also note that typical dynamical time scales, which are of the order of the ratio of the scale height to the local sound speed, are long compared with τ_F. Thus, the neglect of the time-dependent term in the transfer equation is justified. The radiation field adjusts "instantly" to the state of the medium when viewed on a time scale for significant changes in the state of the gas. We observe that $\tau_{th}/\tau_F < 1$ for typical densities in planetary nebulae and the Crab Nebula, suggesting that the time dependence of the mean intensity of the radiation field may be important in these objects.

We next considered the validity of a single temperature for the neutral atoms, ions, and electrons. Electrons are produced by radiative and collisional ionization and removed from the gas by radiative and three-body recombinations. Inelastic collisions and recombinations hinder the achievement of a Maxwellian velocity distribution because they involve electrons only in certain velocity ranges and shift electrons from these ranges to much lower velocities. Elastic self-collisions redistribute energy and tend to produce a Maxwellian velocity distribution at some local electron kinetic temperature. When the gas is not in LTE, the electron velocity will be Maxwellian if the elastic self-collision time is short compared with times for inelastic processes.

We now examine the various relaxation times. The elastic self-collision time (Zel'dovich and Raizer 1967) is

$$\tau_{coll} = \frac{A^{1/2} T^{3/2}}{8.8 \times 10^{-2} N Z^4 \ln \Lambda} ,$$

where A is the atomic weight of particles, N is the density of interacting particles, and $\ln \Lambda \approx 10$ is the far-collision factor.

TABLE 3

RATIO OF THERMAL RELAXATION TO PHOTON FLIGHT TIMES

Position	T	b_1	N	τ_{th}/τ_F
Bottom.....	10^4	1	1.2×10^{13}	4×10^3
Shock.....	3×10^4	10^6	1.2×10^{11}	10^3
Surface.....	10^4	10^2	1.2×10^9	4×10^1

Let us evaluate the elastic self-collision time for electrons and ions behind the shock front, when the shock is in the outer layers of the atmosphere where the temperature is high, $T = 3.36 \times 10^4$ K, and the density is low, $n_e = 3.94 \times 10^{10}$. For electron-electron collisions, with $A = 1/1836$ and $Z = 1$,

$$\tau_{e\text{-}e} = \frac{2.6 \times 10^{-1} T^{3/2}}{n_e \ln \Lambda} = 4.1 \times 10^{-6} \text{ s} .$$

For ion-ion collisions,

$$\tau_{i\text{-}i} = \left(\frac{A_i}{A_e}\right)^{1/2} \tau_{e\text{-}e} = 1.6 \times 10^{-4} \text{ s} .$$

We compare these elastic self-collision times with the time for collisional ionization,

$$\tau_{\text{coll-ion}} \sim \frac{1}{C_{1K}} = 3 \times 10^{-1} \text{ s};$$

the time for radiative recombination,

$$\tau_{\text{rad-rec}} \sim \frac{n_e}{n_1^* R_{K1}} = 2.8 \times 10^2 \text{ s};$$

the time for radiative ionization,

$$\tau_{\text{rad-ion}} \sim \frac{1}{R_{1K}} = 2.6 \times 10^{-1} \text{ s};$$

and the dynamical time scale,

$$\tau_{\text{dyn}} \sim \frac{\text{scale height}}{\text{sound speed}} = 10 \text{ s} .$$

It is apparent that a Maxwellian distribution in the electron and ion gases is established rapidly in comparison with the time it takes other processes to affect such a distribution. Each gas thus establishes its own local kinetic temperature.

The situation is different for establishing equipartition between the electrons and protons. When a shock propagates through a collisional plasma, it heats mainly the ions. The gradual energy transfer from the ions to the electrons by elastic electron-ion collisions brings the electron and ion temperatures into equilibrium downstream of the shock. When interacting particles have very different masses, the kinetic energy transferred by a collision cannot exceed a fraction of the order of the mass ratio—in the present case, m_e/m_{H}. Therefore, appreciable energy transfer requires m_{H}/m_e collisions. The time for energy exchange between ions and electrons is (Zel'dovich and Raizer 1967)

$$\tau_{e\text{-}i} = \frac{2.52 \times 10^2 A T^{3/2}}{N Z^2 \ln \Lambda} ,$$

where N is the ion number density. For the same conditions in the shock as before, $\tau_{e\text{-}i} = 3.9 \times 10^{-3}$ s.

Electrons and ions have the same temperature if the elastic electron-ion exchange time $\tau_{e\text{-}i}$ is very short compared to $\tau_{\text{coll-ion}}$ and $\tau_{\text{rad-rec}}$. Recall that $\tau_{\text{coll-ion}} = 3 \times 10^{-1}$ s and $\tau_{\text{rad-rec}} = 2.8 \times 10^2$ s; hence, we can consider the electron and ion gases to have a common kinetic temperature. The distance $\tau_{e\text{-}i}$ downstream of the shock front where the temperature equilibration of electrons and ions takes place is

$$\lambda_{e\text{-}i} \sim U_S \tau_{e\text{-}i} = 4 \times 10^3 \text{ cm} ,$$

where U_S is the shock velocity. Zones are approximately 10^6 cm thick. It would not be possible to resolve the separate temperatures unless we used a much finer grid spacing.

If sufficiently high temperatures are attained at the shock, $\tau_{e\text{-}i}$ may become comparable to or greater than $\tau_{\text{coll-ion}}$ and $\tau_{\text{rad-rec}}$. In this instance, it may be important to consider separate temperatures for ions and electrons.

Cannon (1974*b*) solved the coupled equations of hydrodynamics and radiative transfer for the continuum by assuming different temperatures for the electron gas and the atom-ion gas. His calculations showed a marked difference in the resulting temperature distributions of the electrons and the heavier particles (atoms and ions) over the shock thickness. He concluded that the temperature difference between the electrons and atoms will be significant in computing the time development of radiative fluxes in spectral lines emerging from stellar surfaces. Our results show that for continuum radiation this is not true. The equilibration time for the electron gas and the atom-ion gas is significantly shorter than any of the radiative or collisional ionization and recombination times. Thus, we conclude that the temperatures will have equilibrated well before the processes that influence the emergent continuum radiation occur; hence, in our case, it is not necessary to take the different temperatures into account.

REFERENCES

Auer, L. 1967, *Ap. J. (Letters)*, **150**, L53.
Auer, L., and Mihalas, D. 1969, *Ap. J.*, **158**, 641.
Baldwin, B. S., and Heaslet, M. A. 1963, *Phys. Fluids*, **6**, 781.
Bopp, B. W., and Moffett, T. J. 1973, *Ap. J.*, **185**, 239.
Cannon, C. J. 1974*a*, *J. Quant. Spectrosc. and Rad. Transf.*, **14**, 745.
———. 1974*b*, *ibid*, p. 760.
Cayrel, R. 1963, *C.R. Acad. Sci. Paris*, **257**, 3309.
Christy, R. F. 1964, *Rev. Mod. Phys.*, **36**, 555.
Feautrier, P. 1964, *C.R. Acad. Sci. Paris*, **258**, 3189.
Hill, S. J. 1972, *Ap. J.*, **178**, 793.
Kahn, F. D. 1954, *B.A.N.*, **12**, 187.
Kalkofen, W. 1968, *Ap. J.*, **151**, 317.
Kalkofen, W., and Whitney, C. 1971, *J. Quant. Spectrosc. and Rad. Transf.*, **11**, 531.
Nelson, H. F., and Goulard, R. 1969, *Phys. Fluids*, **12**, 1605.
Richtmyer, R. D., and Morton, K. W. 1967, *Difference Methods for Initial Value Problems* (New York-Interscience).
Vincenti, W. G., and Baldwin, B. S. 1962, *J. Fluid Mech.*, **12**, 449.
Whitney, C. A., and Skalafuris, A. J. 1963, *Ap. J.*, **138**, 200.
Zel'dovich, Ya. B., and Raizer, Y. P. 1967, *Physics of Shock Waves and High Temperature Hydrodynamic Phenomena* (New York: Academic Press), Vol. **2**.

WOLFGANG KALKOFEN: Center for Astrophysics, Harvard College and Smithsonian Astrophysical Observatory, Cambridge, MA 02138

RICHARD I. KLEIN and ROBERT F. STEIN: Joint Institute for Laboratory Astrophysics, University of Colorado and National Bureau of Standards, Boulder, CO 80302